

# PSEUDOGAPS AND MAGNETIC PROPERTIES OF THE TWO-DIMENSIONAL $t$ - $J$ MODEL

A. Sherman<sup>a</sup> and M. Schreiber<sup>b</sup>

<sup>a</sup>Institute of Physics, University of Tartu, Riia 142, EE-2400 Tartu, Estonia

<sup>b</sup>Institut für Physik, Technische Universität, D-09107 Chemnitz, Germany

## I. INTRODUCTION

The photoemission and magnetic properties of cuprate perovskites have been extensively studied during the last few years, both because of their unusual behaviour and in the hope that they might provide insight into the physical origin of high-temperature superconductivity. Among these properties the pseudogap observed in photoemission [1–3] and the magnetic pseudogap revealed in the static susceptibility and in the spin-lattice relaxation rate of normal-state underdoped cuprates [4,5] have attracted considerable attention. A number of different approaches were suggested for the description of the pseudogaps. In particular, in view of the similarity in symmetry and size of the photoemission pseudogap with the superconducting gap, in Refs. [3,6–8] this pseudogap was connected with the superconducting fluctuations existing above  $T_c$ . This idea was based on earlier theoretical results of Refs. [9,10]. Another point of view was suggested in Ref. [11] where the energy spectrum of the two-dimensional (2D)  $t$ - $J$  model was shown to have a peculiarity which is similar by its properties to the photoemission pseudogap. In accord with Ref. [11] the pseudogap is a consequence of a specific dispersion of the strongly correlated electron system at moderate doping and is not connected with superconducting fluctuations. The discussion of the magnetic pseudogap in doped cuprates is mainly based on scaling arguments [12–14] and on the idea of real-space pairing [15].

In this paper we describe the energy spectrum, including the photoemission pseudogap, and the magnetic properties demonstrating the magnetic pseudogap in a unified approach based on the 2D  $t$ - $J$  model widely used for the description of  $\text{CuO}_2$  planes of cuprate perovskites (the extensive literature on this model is reviewed in Ref. [16]). For the consideration of the paramagnetic state we extend the spin-wave theory with

the constraint of zero staggered magnetization, developed for the Heisenberg model [17,18], to the  $t$ - $J$  model. The spectrum is determined by solving numerically a set of self-energy equations for hole and magnon Green's functions in the self-consistent Born approximation with account of the constraint [19]. The constraint can be fulfilled in the ranges of hole concentrations  $0.02 \lesssim x \lesssim 0.17$  and temperatures  $T \lesssim 100$  K. In this region the obtained hole spectrum differs from a conventional metallic spectrum as the quasiparticle weights of states are less than 1 and change with the hole concentration. This leads to the violation of Luttinger's theorem.

The hole spectrum consists of two essentially different parts: a persistent portion of the narrow spin-polaron band, which is typical for the low-concentration ( $x \lesssim 0.02$ ) spectrum, and a wider part appearing from  $x \approx 0.04$  which is characterized by the energy parameter  $t$ , the hopping constant. The former part provides the most intensive features in the hole spectral function near the Fermi level. For  $x < 0.17$  this part, which is pinned to the Fermi level near  $(\pm\pi/2, \pm\pi/2)$ , bends upwards (in the hole picture) on approaching  $(\pm\pi, 0)$ ,  $(0, \pm\pi)$ . In the hole spectral function the crossing of the Fermi level by the second, wider part is completely lost within the foot of a more intensive spin-polaron peak in this region of the Brillouin zone. This looks like the disappearance of a part of the Fermi surface and the opening of a pseudogap near  $(\pm\pi, 0)$ ,  $(0, \pm\pi)$ . Obtained size, symmetry and concentration dependence of the pseudogap are in agreement with photoemission data in  $\text{Bi}_2\text{Sr}_2\text{CaCu}_2\text{O}_{8+\delta}$  ( $\text{Bi}2212$ ) [1–3].

Another peculiarity of the calculated hole spectrum is an extended saddle point near  $(0, \pi)$ . By the energy position and by the extension in the Brillouin zone our results reproduce well the analogous feature of the photoemission spectra. In the case of optimal doping,  $x \approx 0.17$ , this peculiarity leads to a 2D Fermi surface in the considered 2D system.

A gap in the magnon spectrum of the undoped antiferromagnet appears as a consequence of the constraint of zero staggered magnetization [17,18]. Starting from  $x \approx 0.02$  this gap is filled by overdamped magnons. Their increased damping is the consequence of the hole-magnon interaction and at  $T = 0$  it indicates the destruction of the long-range antiferromagnetic order by holes [20]. The arising pseudogap leads to the decrease of the static spin susceptibility and the spin-lattice relaxation rate  $(T_1 T)^{-1}$  with decreasing temperature, as observed experimentally. This behavior is typical for the quantum disordered regime. Calculated values of these quantities are in qualitative and in some cases in quantitative agreement with experiment in underdoped  $\text{YBa}_2\text{Cu}_3\text{O}_{6+\delta}$ . In some articles the photoemission and magnetic pseudogaps are identified (see, e.g., Ref. [3]). In our opinion these pseudogaps are two different, unconnected peculiarities of the spectra of two well-distinguishable subsystems — holes and magnons.

The outline of the paper is as follows. In Sec. II we discuss the derivation of the  $t$ - $J$  Hamiltonian from the extended Hubbard Hamiltonian which is supposed to give a realistic description of  $\text{CuO}_2$  planes. This allows us to rewrite spin operators of oxygen and copper ions in terms of operators of the  $t$ - $J$  model. The extension of the modified spin-wave approximation with zero staggered magnetization on the  $t$ - $J$  model is discussed in Sec. III. The self-energy equations for the hole and magnon Green's functions and the hole and magnon contributions to the magnetic susceptibility in

terms of these functions are written out in Sec. IV. Numerical results on the spectrum are considered in Sec. V. The pseudogap in the hole spectrum and magnetic properties are discussed in Sec. VI and VII, respectively. Finally our conclusions are given in Sec. VIII.

## II. THE EFFECTIVE HAMILTONIAN

The extended Hubbard model [21] is widely used for the description of  $\text{CuO}_2$  planes of cuprate perovskites. The Hamiltonian of the model can be written in the form [22]

$$\begin{aligned} H &= \sum_{\mathbf{m}} H_{\mathbf{m}} + 2t_{pd}\lambda_{\mathbf{a}} \sum_{\mathbf{m}\mathbf{a}\sigma} (d_{\mathbf{m}\sigma}^\dagger \phi_{\mathbf{m}+\mathbf{a},\sigma} + \text{H.c.}), \\ H_{\mathbf{m}} &= Un_{\mathbf{m},+1}n_{\mathbf{m},-1} + \Delta \sum_{\sigma} \phi_{\mathbf{m}\sigma}^\dagger \phi_{\mathbf{m}\sigma} + 2t_{pd}\lambda_0 \sum_{\sigma} (d_{\mathbf{m}\sigma}^\dagger \phi_{\mathbf{m}\sigma} + \text{H.c.}), \end{aligned} \quad (1)$$

where  $d_{\mathbf{m}\sigma}^\dagger$  is the creation operator of electrons in the  $3d_{x^2-y^2}$  orbitals of copper at the plane site  $\mathbf{m}$  with the spin  $\sigma = \pm 1$ ,  $\phi_{\mathbf{m}\sigma}^\dagger$  is the Fourier transform of the operator  $\phi_{\mathbf{k}\sigma}^\dagger = (\beta_{\mathbf{k}}/2\sqrt{N}) \sum_{\mathbf{m}\mathbf{a}} \exp(-i\mathbf{k}\mathbf{m}) p_{\mathbf{m}+\mathbf{a}/2,\sigma}^\dagger$  constructed from the creation operators of electrons in the  $2p_\sigma$  orbitals of oxygen  $p_{\mathbf{m}+\mathbf{a}/2,\sigma}^\dagger$ . Complementary linear combinations of these operators, which do not hybridize with the  $3d_{x^2-y^2}$  copper orbitals, are omitted in Eq. (1) because their energy is much higher. In Eq. (1),  $\mathbf{a} = (\pm a, 0), (0, \pm a)$  where  $a$  is the in-plane copper distance which is taken as the unit of length,  $\beta_{\mathbf{k}} = \{1 + [\cos(k_x) + \cos(k_y)]/2\}^{-1/2}$ ,  $N$  is the number of sites;  $U$ ,  $\Delta$ , and  $t_{pd}$  are the Hubbard repulsion on copper, the Cu-O promotion energy and hybridization, respectively,  $n_{\mathbf{m}\sigma} = d_{\mathbf{m}\sigma}^\dagger d_{\mathbf{m}\sigma}$ ,  $\lambda_{\mathbf{m}} = N^{-1} \sum_{\mathbf{k}} \exp(i\mathbf{k}\mathbf{m}) \beta_{\mathbf{k}}^{-1}$ ,  $\lambda_0 \approx 0.96$ ,  $\lambda_{\mathbf{a}} \approx 0.14$ . Other components of  $\lambda_{\mathbf{m}}$  are small and the respective terms are omitted in Eq. (1).

The splitting of the Hamiltonian into the one- and two-site parts in Eq. (1) provides a good starting point for the perturbation theory, because for parameters [23] of  $\text{La}_2\text{CuO}_4$  these two parts are characterized by energies differing by one order of magnitude. Notice that the frequently used perturbation expansion in powers of  $t_{pd}$  does not work for these parameters, as the hybridization is actually not small in comparison with other energies [22,24]. The prefactor  $\lambda_{\mathbf{a}} \sim 0.1$  in Eq. (1) allows one to overcome this difficulty. The zero-order, one-site part  $\sum_{\mathbf{m}} H_{\mathbf{m}}$  of the Hamiltonian has two sets of states corresponding to unoccupied and occupied site states of the  $t$ - $J$  model

$$\begin{aligned} |\mathbf{m}\rangle &= \left[ \frac{c_{21}}{\sqrt{2}} (\phi_{\mathbf{m},+1}^\dagger d_{\mathbf{m},-1}^\dagger - \phi_{\mathbf{m},-1}^\dagger d_{\mathbf{m},+1}^\dagger) + c_{22} \phi_{\mathbf{m},-1}^\dagger \phi_{\mathbf{m},+1}^\dagger + c_{23} d_{\mathbf{m},-1}^\dagger d_{\mathbf{m},+1}^\dagger \right] |v_{\mathbf{m}}\rangle, \\ |\mathbf{m}\sigma\rangle &= (c_{31} \phi_{\mathbf{m},-1}^\dagger \phi_{\mathbf{m},+1}^\dagger d_{\mathbf{m}\sigma}^\dagger + c_{32} \phi_{\mathbf{m}\sigma}^\dagger d_{\mathbf{m},-1}^\dagger d_{\mathbf{m},+1}^\dagger) |v_{\mathbf{m}}\rangle, \end{aligned} \quad (2)$$

where  $|v_{\mathbf{m}}\rangle$  is the site vacuum state and the coefficients  $c_{ij}$  are obtained in the course of the diagonalization of  $H_{\mathbf{m}}$ . For a given number of holes crystal states  $|q\rangle$  constructed as products of site states (2) form the degenerate ground states of the zero-order Hamiltonian  $H_0 = \sum_{\mathbf{m}} H_{\mathbf{m}}$ . These ground states are separated by a finite gap of the order of  $\min(\Delta, t_{pd})$  from excited states. In such conditions one can use the operator form of the perturbation theory [25] to obtain an effective Hamiltonian acting in the subspace

of the low-lying states  $|q\rangle$ . Up to the terms of the second order in the perturbation  $H_1$  [the two-site part of Hamiltonian (1)] this effective Hamiltonian reads

$$H_{\text{eff}} = \mathcal{P}[H_1 - H_1(1 - \mathcal{P})(H_0 - E_0)^{-1}(1 - \mathcal{P})H_1]\mathcal{P},$$

where  $\mathcal{P} = \sum_q |q\rangle\langle q|$  and  $E_0$  is the eigenenergy of  $H_0$  for the ground states  $|q\rangle$ . Using Eqs. (1) and (2) we obtain the effective  $t$ - $J$  Hamiltonian [22]

$$H_{\text{eff}} = t \sum_{\mathbf{m}\mathbf{a}\sigma} |\mathbf{m} + \mathbf{a}, \sigma\rangle\langle \mathbf{m} + \mathbf{a}| |\mathbf{m}\rangle\langle \mathbf{m}\sigma| + \frac{J}{2} \sum_{\mathbf{m}\mathbf{a}} \mathbf{S}_{\mathbf{m}} \mathbf{S}_{\mathbf{m}+\mathbf{a}}, \quad (3)$$

where  $S_{\mathbf{m}}^{\sigma} = S_{\mathbf{m}}^x + i\sigma S_{\mathbf{m}}^y = |\mathbf{m}\sigma\rangle\langle \mathbf{m}, -\sigma|$ ,  $S_{\mathbf{m}}^z = \sum_{\sigma} (\sigma/2) |\mathbf{m}\sigma\rangle\langle \mathbf{m}\sigma|$  are the components of the spin operator  $\mathbf{S}_{\mathbf{m}}$ ,  $t$  and  $J$  are the effective hopping and superexchange constants which are expressed in terms of the parameters of the extended Hubbard Hamiltonian [see Ref. [22]; in Eq. (3), we omitted three-site ( $t'$ ) terms which give only small corrections in the considered case  $J/t \ll 1$ ]. Using parameters of Ref. [23] we estimated the ratio  $J/t$  to lie in the range 0.1–0.5. In the following discussion we use  $J/t = 0.2$  and  $t = 0.5$  eV.

The Zeeman term of the Hamiltonian can be written in the form

$$H_Z = 2\mu_B \sum_{\mathbf{m}} \mathbf{s}_{\mathbf{m}} \mathbf{H}_{\mathbf{m}} + \mu_B \sum_{\mathbf{m}\mathbf{a}} \mathbf{s}_{\mathbf{m}+\mathbf{a}/2} \mathbf{H}_{\mathbf{m}+\mathbf{a}/2}, \quad (4)$$

where  $\mu_B$  is the Bohr magneton,  $\mathbf{H}_{\mathbf{m}}$  is the applied magnetic field, and  $\mathbf{s}_{\mathbf{m}}$  and  $\mathbf{s}_{\mathbf{m}+\mathbf{a}/2}$  are composed of

$$\begin{aligned} s_{\mathbf{m}}^{\sigma} &= d_{\mathbf{m}\sigma}^{\dagger} d_{\mathbf{m}, -\sigma}, & s_{\mathbf{m}}^z &= \sum_{\sigma} \frac{\sigma}{2} d_{\mathbf{m}\sigma}^{\dagger} d_{\mathbf{m}\sigma}, \\ s_{\mathbf{m}+\mathbf{a}/2}^{\sigma} &= p_{\mathbf{m}+\mathbf{a}/2, \sigma}^{\dagger} p_{\mathbf{m}+\mathbf{a}/2, -\sigma}, & s_{\mathbf{m}+\mathbf{a}/2}^z &= \sum_{\sigma} \frac{\sigma}{2} p_{\mathbf{m}+\mathbf{a}/2, \sigma}^{\dagger} p_{\mathbf{m}+\mathbf{a}/2, \sigma}, \end{aligned}$$

respectively. Using notations of Eq. (1) the oxygen spin operators can be approximately rewritten as

$$\begin{aligned} s_{\mathbf{m}+\mathbf{a}/2}^{\sigma} &= \frac{\tilde{\beta}^2}{4} (\phi_{\mathbf{m}\sigma}^{\dagger} + \phi_{\mathbf{m}+\mathbf{a}, \sigma}^{\dagger}) (\phi_{\mathbf{m}, -\sigma} + \phi_{\mathbf{m}+\mathbf{a}, -\sigma}), \\ s_{\mathbf{m}+\mathbf{a}/2}^z &= \frac{\tilde{\beta}^2}{8} \sum_{\sigma} \sigma (\phi_{\mathbf{m}\sigma}^{\dagger} + \phi_{\mathbf{m}+\mathbf{a}, \sigma}^{\dagger}) (\phi_{\mathbf{m}\sigma} + \phi_{\mathbf{m}+\mathbf{a}, \sigma}), \end{aligned} \quad (5)$$

where  $\tilde{\beta} = \beta_0 + \beta_{\mathbf{a}} \approx 0.96$ ,  $\beta_{\mathbf{m}}$  being the Fourier transform of  $\beta_{\mathbf{k}}$ . In the basis of states (2) the spin operators read

$$\begin{aligned} s_{\mathbf{m}+\mathbf{a}/2}^z &= c_{21}^2 c_{31}^2 \tilde{\beta}^2 \sum_{\sigma} \frac{\sigma}{16} (|\mathbf{m}\sigma\rangle\langle \mathbf{m}| |\mathbf{m} + \mathbf{a}\rangle\langle \mathbf{m} + \mathbf{a}, \sigma| \\ &\quad + |\mathbf{m} + \mathbf{a}, \sigma\rangle\langle \mathbf{m} + \mathbf{a}| |\mathbf{m}\rangle\langle \mathbf{m}\sigma|), \\ s_{\mathbf{m}}^z &= c_{31}^2 \sum_{\sigma} \frac{\sigma}{2} |\mathbf{m}\sigma\rangle\langle \mathbf{m}\sigma|, \end{aligned} \quad (6)$$

where in the oxygen operator terms containing small coefficients  $c_{32}$ ,  $c_{23}$  were omitted. In the following discussion we set  $c_{21} = c_{31} = \tilde{\beta} = 1$ .

### III. THE SPIN-WAVE APPROXIMATION FOR ZERO STAGGERED MAGNETIZATION

Hamiltonian (3) can be essentially simplified with the use of the spin-wave approximation. As known [26], at low temperatures and hole concentrations  $x \lesssim 0.02$  the  $\text{CuO}_2$  planes are antiferromagnetically ordered. For larger  $x$  this long-range ordering is destroyed. To describe low-lying magnetic excitations and their interaction with holes in this case we use the version of the spin-wave theory formulated in Refs. [17,18] for the Heisenberg antiferromagnet with zero staggered magnetization. As shown in Refs. [17,18], in the absence of holes this approach reproduces results obtained in Refs. [27,28] with the mean-field Schwinger boson and renormalization group theories and it is remarkably accurate, as follows from the comparison with exact diagonalization and Monte Carlo results. Here we reformulate this approach to simplify the inclusion of holes in the Hamiltonian.

We use the Holstein-Primakoff transformation [25] to introduce boson operators of spin waves  $b_{\mathbf{m}}$ ,

$$S_{\mathbf{m}}^z = e^{i\mathbf{\Pi}\mathbf{m}} \left( \frac{1}{2} - b_{\mathbf{m}}^\dagger b_{\mathbf{m}} \right), \quad S_{\mathbf{m}}^\sigma = P_{\mathbf{m}}^\sigma \varphi_{\mathbf{m}} b_{\mathbf{m}} + P_{\mathbf{m}}^{-\sigma} b_{\mathbf{m}}^\dagger \varphi_{\mathbf{m}}, \quad (7)$$

where  $\mathbf{\Pi} = (\pi, \pi)$ ,  $P_{\mathbf{m}}^\sigma = [1 + \sigma \exp(i\mathbf{\Pi}\mathbf{m})]/2$ , and  $\varphi_{\mathbf{m}} = (1 - b_{\mathbf{m}}^\dagger b_{\mathbf{m}})^{1/2}$ . In Eq. (7), the factors  $\exp(i\mathbf{\Pi}\mathbf{m})$  and  $P_{\mathbf{m}}^{\pm\sigma}$  are introduced to account for alternating directions of spins in the classical Néel state which is used as the reference state in the spin-wave approximation. On substituting Eq. (7) into the Heisenberg part of Hamiltonian (3), expanding  $\varphi_{\mathbf{m}}$  and keeping terms up to the quartic order, we use the mean-field approximation in these latter terms

$$H_H = \frac{J}{2} \sum_{\mathbf{m}\mathbf{a}} \mathbf{S}_{\mathbf{m}+\mathbf{a}} \mathbf{S}_{\mathbf{m}} \approx -\frac{JN}{2} - J\langle b_0 b_{\mathbf{a}} \rangle \left[ 4 \sum_{\mathbf{m}} b_{\mathbf{m}}^\dagger b_{\mathbf{m}} + \frac{1}{2} \sum_{\mathbf{m}\mathbf{a}} (b_{\mathbf{m}+\mathbf{a}}^\dagger b_{\mathbf{m}}^\dagger + b_{\mathbf{m}+\mathbf{a}} b_{\mathbf{m}}) \right], \quad (8)$$

where angular brackets denote averaging over the grand canonical ensemble and the four correlations  $\langle b_0 b_{\mathbf{a}} \rangle$  are supposed to be equal. On deriving Eq. (8) we took into account the condition

$$\langle b_{\mathbf{m}}^\dagger b_{\mathbf{m}} \rangle = \frac{1}{2} \quad (9a)$$

which follows from the constraint of zero staggered magnetization,

$$\sum_{\mathbf{m}} e^{i\mathbf{\Pi}\mathbf{m}} S_{\mathbf{m}}^z = 0 \quad \text{or} \quad \sum_{\mathbf{m}} b_{\mathbf{m}}^\dagger b_{\mathbf{m}} = \frac{N}{2} \quad (9b)$$

and ensures zero site magnetization,  $\langle S_{\mathbf{m}}^z \rangle = 0$ . To account for this constraint in the subsequent consideration we add the term  $2J\nu\langle b_0 b_{\mathbf{a}} \rangle \sum_{\mathbf{m}} b_{\mathbf{m}}^\dagger b_{\mathbf{m}}$  with the Lagrange multiplier  $\nu$  to Hamiltonian (8).

The deviation of the quartic terms from their mean-field value in Eq. (8) describes the magnon-magnon interaction which leads to the magnon damping [29]. In the  $t$ - $J$  model there is another mechanism of the magnon damping connected with the

hole-magnon interaction. Estimations [20,29] show that in the considered range of hole concentrations this latter interaction gives the main contribution to the damping. Therefore we do not consider the magnon-magnon interaction below.

The resulting Hamiltonian is diagonalized by the unitary transformation

$$U = \exp \left[ \frac{1}{2} \sum'_{\mathbf{k}\sigma} \alpha_{\mathbf{k}} (b_{\mathbf{k}\sigma} b_{-\mathbf{k},-\sigma} - b_{\mathbf{k}\sigma}^\dagger b_{-\mathbf{k},-\sigma}^\dagger) \right] \quad (10)$$

with  $\alpha_{\mathbf{k}} = \ln[(1+\eta\gamma_{\mathbf{k}})/(1-\eta\gamma_{\mathbf{k}})]/4$ ,  $\eta = 2/(2-\nu)$ ,  $\gamma_{\mathbf{k}} = \sum_{\mathbf{a}} \exp(i\mathbf{k}\mathbf{a})/4$ , and the primed sum sign indicates that the summation is restricted to the magnetic Brillouin zone which is half as large as the usual one. In Eq. (10),  $b_{\mathbf{k}\sigma} = \sqrt{2/N} \sum_{\mathbf{m}} \exp(-i\mathbf{k}\mathbf{m}) b_{\mathbf{m}} P_{\mathbf{m}}^\sigma$  where due to the projector  $P_{\mathbf{m}}^\sigma$  the summation is performed over one sublattice. As a result, we obtain

$$\begin{aligned} \mathcal{H}_H &= U^\dagger H_H U = \sum'_{\mathbf{k}\sigma} \omega_{\mathbf{k}}^0 b_{\mathbf{k}\sigma}^\dagger b_{\mathbf{k}\sigma}, \quad \omega_{\mathbf{k}}^0 = -\frac{4J}{\eta} \langle b_0 b_{\mathbf{a}} \rangle \sqrt{1 - \eta^2 \gamma_{\mathbf{k}}^2}, \\ \langle b_0 b_{\mathbf{a}} \rangle &= \frac{2}{N} \sum'_{\mathbf{k}\sigma} \frac{\gamma_{\mathbf{k}}}{\sqrt{1 - \eta^2 \gamma_{\mathbf{k}}^2}} \left[ \langle b_{-\mathbf{k},-\sigma} b_{\mathbf{k}\sigma} \rangle_U - \eta \gamma_{\mathbf{k}} \left( \langle b_{\mathbf{k}\sigma}^\dagger b_{\mathbf{k}\sigma} \rangle_U + \frac{1}{2} \right) \right], \end{aligned} \quad (11)$$

where we omitted unessential constant terms, and in  $\langle b_0 b_{\mathbf{a}} \rangle$  for the following discussion we keep the anomalous correlation  $\langle b_{-\mathbf{k},-\sigma} b_{\mathbf{k}\sigma} \rangle_U$  which is nonzero at  $x \neq 0$ . The subscript  $U$  means that the averaging is performed with the Hamiltonian transformed with operator (10). In the absence of holes we have  $\langle b_{\mathbf{k}\sigma}^\dagger b_{\mathbf{k}\sigma} \rangle_U = [\exp(\omega_{\mathbf{k}}^0/T) - 1]^{-1}$  and  $\langle b_{-\mathbf{k},-\sigma} b_{\mathbf{k}\sigma} \rangle_U = 0$  where  $T$  is the temperature in energy units, while for  $x > 0$  the correlations are calculated from the magnon Green's function. Condition (9a) which determines  $\eta$  in Eq. (11) acquires the form

$$\frac{2}{N} \sum'_{\mathbf{k}} \frac{1}{\sqrt{1 - \eta^2 \gamma_{\mathbf{k}}^2}} \left( \langle b_{\mathbf{k}\sigma}^\dagger b_{\mathbf{k}\sigma} \rangle_U + \frac{1}{2} - \eta \gamma_{\mathbf{k}} \langle b_{-\mathbf{k},-\sigma} b_{\mathbf{k}\sigma} \rangle_U \right) = 1. \quad (12)$$

Analogous equations (without  $\langle b_{-\mathbf{k},-\sigma} b_{\mathbf{k}\sigma} \rangle_U$ ) for the magnon spectrum of the Heisenberg antiferromagnet without holes were obtained in a somewhat different manner in Refs. [17,18]. As shown in these works, in states without long-range antiferromagnetic ordering and for finite lattices one obtains  $\eta < 1$  which introduces a gap in the magnon spectrum (11) near the points  $(0,0)$  and  $(\pi,\pi)$  of the Brillouin zone.

The reference state of the spin-wave approximation discussed above is the classical Néel state  $|\mathcal{N}\rangle$ . Other states are described via the reference state and magnon creation operators determined for this state. The introduction of holes in this picture leads to two possibilities for the hole movement: there is a magnon or there is no magnon on a site which a hole jumps to. Both these possibilities are described by the following term of the Hamiltonian:

$$H_t = t \sum_{\mathbf{m}\mathbf{a}} h_{\mathbf{m}} h_{\mathbf{m}+\mathbf{a}}^\dagger (b_{\mathbf{m}+\mathbf{a}} + b_{\mathbf{m}}^\dagger), \quad (13)$$

which corresponds to the first term in Eq. (3). In Eq. (13),  $h_{\mathbf{m}}^\dagger = \sum_{\sigma} P_{\mathbf{m}}^\sigma |\mathbf{m}\rangle \langle \mathbf{m}\sigma|$  is the hole creation operator in the Néel state  $|\mathcal{N}\rangle = \prod_{\mathbf{m}} (\sum_{\sigma} P_{\mathbf{m}}^\sigma |\mathbf{m}\sigma\rangle)$ .

In spite of the clear physical meaning of the constraint of zero staggered magnetization, let us discuss the approximations made from a somewhat different point of view. Notice that in the case of short-range antiferromagnetic order characterized by the spin correlation length  $\xi \gg a$  one can use the usual spin-wave approximation in any crystal region with a linear size of the order of  $\xi$ . A Néel state with some local spin quantization axis is used as the reference state for this spin-wave approximation. Additionally one should take into account the finite-size effect due to a finite value of  $\xi$ . This is done by applying condition (12). The value of  $\eta$  determined by this condition is directly connected with  $\xi$  [17] (recall that  $\eta < 1$  both for a finite  $\xi$  and a finite lattice). Notice also that only sites neighboring to the hole site are involved in the processes described by Eq. (13). The hole-magnon interaction is of the short-range type. This is the reason why in the case of short-range antiferromagnetic order with  $\xi \gg a$  the hole hopping term (13) looks exactly like the same term for the long-range order [30,31]. There is no “bare-hopping” (without magnon operators) term in Eq. (13) because in the case  $\xi \gg a$  the direction of the spin quantization axis is practically the same on sites involved in a hole jump.

After unitary transformation (10) the total Hamiltonian reads

$$\mathcal{H} = U^\dagger H_t U + \mathcal{H}_H = \sum'_{\mathbf{k}\mathbf{k}'\sigma} (g_{\mathbf{k}\mathbf{k}'} h_{\mathbf{k}\sigma}^\dagger h_{\mathbf{k}-\mathbf{k}',-\sigma} b_{\mathbf{k}'\sigma} + \text{H.c.}) + \sum'_{\mathbf{k}\sigma} \omega_{\mathbf{k}}^0 b_{\mathbf{k}\sigma}^\dagger b_{\mathbf{k}\sigma}, \quad (14)$$

where  $g_{\mathbf{k}\mathbf{k}'} = -4t\sqrt{2/N}(\gamma_{\mathbf{k}-\mathbf{k}'}u_{\mathbf{k}'} + \gamma_{\mathbf{k}}v_{\mathbf{k}'})$  and  $u_{\mathbf{k}} = \cosh(\alpha_{\mathbf{k}})$ ,  $v_{\mathbf{k}} = -\sinh(\alpha_{\mathbf{k}})$ . On carrying out the unitary transformation we neglected the noncommutativity of hole and magnon operators which is justified at least for  $x \lesssim 0.1$  by comparison with exact diagonalization results [32]. At  $\eta = 1$  Eq. (14) reduces to the Hamiltonian obtained in Refs. [30,31] for the case of the long-range antiferromagnetic order. The number of magnons is not conserved by Hamiltonian (14) and at  $x > 0$  the anomalous correlation  $\langle b_{-\mathbf{k},-\sigma} b_{\mathbf{k}\sigma} \rangle_U$  in Eqs. (11) and (12) is nonzero.

Notice that the used spin-wave approximation is not rotationally invariant and the correlations  $\langle S_1^+ S_{\mathbf{m}}^- \rangle$  are zero [17,18]. Therefore only the  $z$  components of spin operators are considered in the following discussion.

#### IV. SUSCEPTIBILITY AND SELF-ENERGY EQUATIONS

In the new notations the spin components (6) acquire the form

$$s_{\mathbf{m}}^z = \frac{1}{2} e^{i\Pi\mathbf{m}} \left( \frac{1}{2} - b_{\mathbf{m}}^\dagger b_{\mathbf{m}} \right), \quad s_{\mathbf{m}+\mathbf{a}/2}^z = \frac{1}{32} e^{i\Pi\mathbf{m}} \left[ h_{\mathbf{m}} h_{\mathbf{m}+\mathbf{a}}^\dagger (b_{\mathbf{m}+\mathbf{a}} - b_{\mathbf{m}}^\dagger) + \text{H.c.} \right]. \quad (15)$$

$s_{\mathbf{m}}^z$  and  $s_{\mathbf{m}+\mathbf{a}/2}^z$  give contributions to the magnetization

$$M_{\mathbf{q}}^z = -2\mu_B s_{\mathbf{q}}^z, \quad s_{\mathbf{q}}^z = \sum_{\mathbf{m}} s_{\mathbf{m}}^z e^{-i\mathbf{q}\mathbf{m}} + \sum_{\mathbf{m}} \sum_{\mathbf{a}'} s_{\mathbf{m}+\mathbf{a}'/2}^z e^{-i\mathbf{q}(\mathbf{m}+\mathbf{a}'/2)},$$

from magnons and holes, respectively. Here  $\mathbf{a}' = (a, 0)$ ,  $(0, a)$ . The susceptibility is determined by the equation

$$\chi^z(\mathbf{q}\omega) = \frac{i}{N} \int_0^\infty d\tau e^{i\omega\tau} \langle [M_{\mathbf{q}\tau}^z, M_{-\mathbf{q}}^z] \rangle,$$

where  $M_{\mathbf{q}\tau}^z = \exp(iH\tau)M_{\mathbf{q}}^z \exp(-iH\tau)$ ,  $H = H_t + H_H - \mu\mathcal{N}$ ,  $\mathcal{N} = \sum_{\mathbf{k}\sigma}' h_{\mathbf{k}\sigma}^\dagger h_{\mathbf{k}\sigma}$ , and  $\mu$  is the hole chemical potential. The susceptibility can be calculated using the simplest decoupling, as the subsequent terms of the perturbation series for the respective Matsubara Green's function are proportional to powers of the small hole concentration and are further decreased by rapidly oscillating coefficients. In this approximation the magnon and hole contributions (indicated by subscripts  $m$  and  $h$ , respectively) in the susceptibility can be written as

$$\begin{aligned}
\text{Im } \chi_m^z(\mathbf{q}\omega) &= \frac{4\mu_B^2}{N} \sum_{\mathbf{k}} \int_{-\infty}^{\infty} \frac{d\nu}{\pi} [n_B(\nu) - n_B(\nu + \omega)] \\
&\quad \times [K_1(\mathbf{k}, \nu) K_1(\mathbf{k} + \boldsymbol{\kappa}, \nu + \omega) + K_2(\mathbf{k}, \nu) K_2(\mathbf{k} + \boldsymbol{\kappa}, \nu + \omega)], \\
\text{Im } \chi_h^z(\mathbf{q}\omega) &= \frac{\mu_B^2}{16N^2} \sum_{\mathbf{k}\mathbf{k}'} \iint_{-\infty}^{\infty} \frac{d\nu d\nu'}{\pi^2} [n_F(\nu) - n_F(\nu + \nu' - \omega)] [n_B(\nu') - n_B(\nu' - \omega)] \\
&\quad \times \text{Im } G(\mathbf{k}\nu) \text{Im } G(\mathbf{k} + \mathbf{k}' - \mathbf{q}, \nu + \nu' - \omega) \\
&\quad \times \left[ \text{Im } D_{11}(\mathbf{k}'\nu') \gamma^2\left(\mathbf{k} - \frac{\mathbf{q}}{2}\right) - \text{Im } D_{11}(\mathbf{k}', -\nu') \gamma^2\left(\mathbf{k} + \mathbf{k}' - \frac{\mathbf{q}}{2}\right) \right. \\
&\quad \left. - 2\text{Im } D_{12}(\mathbf{k}'\nu') \gamma\left(\mathbf{k} - \frac{\mathbf{q}}{2}\right) \gamma\left(\mathbf{k} + \mathbf{k}' - \frac{\mathbf{q}}{2}\right) \right], \\
\text{Re } \chi(\mathbf{q}\omega) &= \mathcal{P} \int_{-\infty}^{\infty} \frac{d\nu}{\pi} \frac{\text{Im } \chi(\mathbf{q}\omega)}{\nu - \omega},
\end{aligned} \tag{16}$$

where  $n_B = [\exp(\omega/T) - 1]^{-1}$ ,  $n_F = [\exp(\omega/T) + 1]^{-1}$ ,  $\boldsymbol{\kappa} = \mathbf{q} - \boldsymbol{\Pi}$ ,

$$K_1(\mathbf{k}\omega) = u_{\mathbf{k}}^2 \text{Im } D_{11}(\mathbf{k}\omega) + 2u_{\mathbf{k}}v_{\mathbf{k}} \text{Im } D_{12}(\mathbf{k}\omega) - v_{\mathbf{k}}^2 \text{Im } D_{11}(\mathbf{k}, -\omega),$$

$$K_2(\mathbf{k}\omega) = u_{\mathbf{k}}v_{\mathbf{k}} [\text{Im } D_{11}(\mathbf{k}\omega) - \text{Im } D_{11}(\mathbf{k}, -\omega)] + (u_{\mathbf{k}}^2 + v_{\mathbf{k}}^2) \text{Im } D_{12}(\mathbf{k}\omega),$$

and  $D_{ij}(\mathbf{k}\omega)$ ,  $G(\mathbf{k}\omega)$  are the Fourier transforms of the magnon and hole Green's functions

$$\begin{aligned}
D_{11}(\mathbf{k}t) &= -i\theta(t) \langle [b_{\mathbf{k}\sigma}(t), b_{\mathbf{k}\sigma}^\dagger] \rangle_U, \quad D_{12}(\mathbf{k}t) = -i\theta(t) \langle [b_{-\mathbf{k}, -\sigma}(t), b_{\mathbf{k}\sigma}] \rangle_U, \\
G(\mathbf{k}t) &= -i\theta(t) \langle [h_{\mathbf{k}\sigma}(t), h_{\mathbf{k}\sigma}^\dagger] \rangle_U,
\end{aligned}$$

$b_{\mathbf{k}\sigma}(t) = \exp[i(\mathcal{H} - \mu\mathcal{N})t] b_{\mathbf{k}\sigma} \exp[-i(\mathcal{H} - \mu\mathcal{N})t]$ . These Green's functions do not depend on the spin index. In Eq. (16), summations over wave vectors are performed over the full Brillouin zone. In the second magnetic zone, which together with the first magnetic zone forms this full zone,  $D_{11}(\mathbf{k}\omega)$  and  $G(\mathbf{k}\omega)$  repeat periodically their values in the first zone, while  $D_{12}(\mathbf{k}\omega)$  changes sign.

These Green's functions are determined from the set of self-energy equations. The hole  $\Sigma$  and magnon  $\Pi_{11}$ ,  $\Pi_{12}$  self-energies are described by the following diagrams:

$$\begin{aligned}
\Sigma &= \text{diagram 1} + \text{diagram 2} + \text{diagram 3} + \text{diagram 4}, \\
\Pi_{11} &= \text{diagram 5}, \quad \Pi_{12} = \text{diagram 6},
\end{aligned}$$



where solid and dashed lines correspond to hole and magnon Green's functions, open and filled circles are bare and full vertices. Dashed lines with two oppositely directed arrows correspond to the anomalous magnon Green's functions  $D_{12}(\mathbf{k}t)$  and  $D_{21}(\mathbf{k}t) = -i\theta(t)\langle[b_{\mathbf{k}\sigma}^\dagger(t), b_{-\mathbf{k},-\sigma}^\dagger]\rangle_U$ . The first correction to the bare vertex  $g_{\mathbf{k}\mathbf{k}'}$  is exactly zero due to the impossibility to coordinate spin indices in this correction [33]. This suggests the use of the Born approximation in which the full vertices are substituted with the bare ones. In this approximation the real-frequency self-energy equations read

$$\begin{aligned}
G(\mathbf{k}\omega) &= [\omega + \mu - \Sigma(\mathbf{k}\omega)]^{-1}, \\
\text{Im } \Sigma(\mathbf{k}\omega) &= -2 \sum'_{\mathbf{k}'} \int_{-\infty}^{\infty} \frac{d\omega'}{\pi} \left[ g_{\mathbf{k}\mathbf{k}'}^2 \text{Im } D_{11}(\mathbf{k}'\omega') - g_{\mathbf{k}-\mathbf{k}',-\mathbf{k}'}^2 \text{Im } D_{11}(-\mathbf{k}', -\omega') \right. \\
&\quad \left. + 2g_{\mathbf{k}\mathbf{k}'}g_{\mathbf{k}-\mathbf{k}',-\mathbf{k}'} \text{Im } D_{12}(\mathbf{k}'\omega') \right] [n_B(\omega') + n_F(\omega' - \omega)] \text{Im } G(\mathbf{k} - \mathbf{k}', \omega - \omega'), \\
\text{Re } \Sigma(\mathbf{k}\omega) &= \mathcal{P} \int_{-\infty}^{\infty} \frac{d\omega'}{\pi} \frac{\text{Im } \Sigma(\mathbf{k}\omega')}{\omega' - \omega}, \\
D_{11}(\mathbf{k}\omega) &= \frac{R^*(\mathbf{k}, -\omega)}{R(\mathbf{k}\omega)R^*(\mathbf{k}, -\omega) - \Pi_{12}^2(\mathbf{k}, \omega)}, \quad D_{12}(\mathbf{k}\omega) = \frac{\Pi_{12}(\mathbf{k}, \omega)}{R(\mathbf{k}\omega)R^*(\mathbf{k}, -\omega) - \Pi_{12}^2(\mathbf{k}, \omega)}, \\
\text{Im } \Pi_{11}(\mathbf{k}\omega) &= 2 \sum'_{\mathbf{k}'} g_{\mathbf{k}'\mathbf{k}}^2 \int_{-\infty}^{\infty} \frac{d\omega'}{\pi} \text{Im } G(\mathbf{k}'\omega') \text{Im } G(\mathbf{k}' - \mathbf{k}, \omega' - \omega) [n_F(\omega') - n_F(\omega' - \omega)], \\
\text{Im } \Pi_{12}(\mathbf{k}\omega) &= 2 \sum'_{\mathbf{k}'} g_{\mathbf{k}'\mathbf{k}}g_{\mathbf{k}'-\mathbf{k},-\mathbf{k}} \int_{-\infty}^{\infty} \frac{d\omega'}{\pi} \text{Im } G(\mathbf{k}'\omega') \text{Im } G(\mathbf{k}' - \mathbf{k}, \omega' - \omega) \\
&\quad \times [n_F(\omega') - n_F(\omega' - \omega)], \\
\text{Re } \Pi_{ij}(\mathbf{k}\omega) &= \mathcal{P} \int_{-\infty}^{\infty} \frac{d\omega'}{\pi} \frac{\text{Im } \Pi_{ij}(\mathbf{k}\omega')}{\omega' - \omega},
\end{aligned} \tag{17}$$

where  $R(\mathbf{k}\omega) = \omega - \omega_{\mathbf{k}}^0 - \Pi_{11}(\mathbf{k}\omega)$ . Equations (17) and (12) form a self-consistent set and can be solved iteratively. The calculation procedure is the following: for given values of  $\mu$  and  $T$  some starting value  $\eta < 1$  was selected; after the convergence of

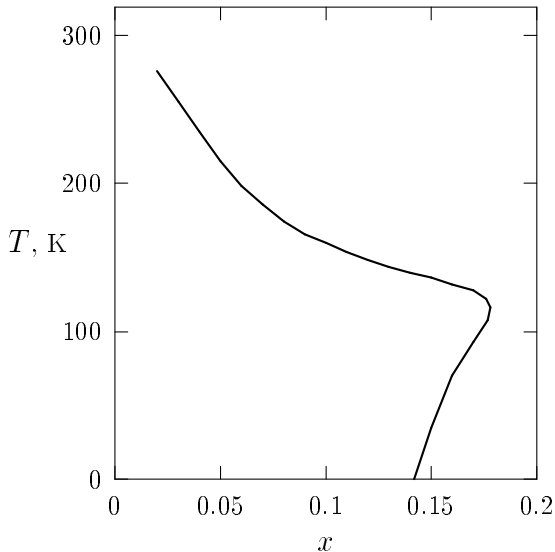


Fig. 1. The curve encloses the region where condition (12) can be fulfilled.

the iterations condition (12) is checked and  $\eta$  is appropriately changed for the next iteration cycle, until the condition is fulfilled with the accuracy of  $10^{-3}$  (some other details of the calculation procedure can be found in Ref. [34]). In the calculations a  $20 \times 20$  lattice was used. Green's functions were computed on a mesh of frequency points equally spaced with the step  $\Delta\omega \approx 0.022t \approx 11$  meV. We found that condition (12) can be satisfied only in a limited region of the  $T$ - $x$  plane, namely below the curve shown in Fig. 1.

## V. THE ENERGY SPECTRUM

The evolution of the calculated hole spectral function  $A(\mathbf{k}\omega) = -\text{Im} G(\mathbf{k}\omega)$  with the concentration

$$x = -\frac{2}{\pi N} \sum_{\mathbf{k}} \int_{-\infty}^{\infty} d\omega n_F(\omega) \text{Im} G(\mathbf{k}\omega) \quad (18)$$

is shown in Fig. 2 for two points of the Brillouin zone. We use the hole picture where

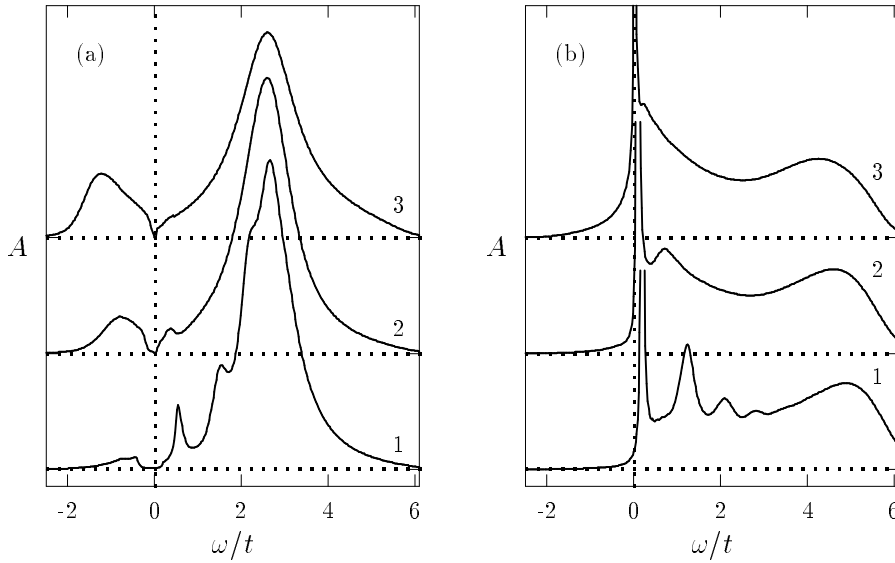


Fig. 2. The hole spectral function  $A(\mathbf{k}\omega)$  for  $\mathbf{k} = (0,0)$  (a) and  $(0,\pi)$  (b).  $T = 0$ . Curves 1, 2, and 3 correspond to  $x = 0.016$ ,  $0.059$ , and  $0.133$ , respectively.

states below the Fermi level  $\omega = 0$  are filled by holes. Since our description is based on the spin-wave approximation with the magnetic Brillouin zone which is twice smaller than the full Brillouin zone, the spectral functions in the points  $\mathbf{k}$  and  $\mathbf{k} + (\pi, \pi)$  are identical. For long-range antiferromagnetic ordering when these points are equivalent such description does not lead to any loss of information. In the case of short-range order the use of the smaller Brillouin zone leads to a somewhat coarsened description. The points  $\mathbf{k}$  and  $\mathbf{k} + (\pi, \pi)$  are no longer equivalent — the respective spectral functions contain similar maxima which however have essentially different intensities and widths [35]. In our approach, where the maxima in the two points appear together in one spectral function for the momentum in the first magnetic Brillouin zone, we cannot

determine whether a selected maximum is more intensive in the first or in the second magnetic Brillouin zone (which form the full zone). In other words we cannot determine where is the usual band and where is the shadow band [35]. However, we can distribute the maxima between the two magnetic zones by drawing additional information from experiment as we shall do in the following discussion.

At  $x \lesssim 0.04$  the spectra contain series of peaks and the hole-magnon scattering continuum (see curves 1 in Fig. 2). With increasing  $x$  only the lowest and most intensive of these peaks is retained in the spectrum for wave vectors near the boundary of the magnetic Brillouin zone [everywhere in this region the spectrum is similar to that for  $\mathbf{k} = (0, \pi)$ ]. This peak corresponds to the so-called spin-polaron band in the hole spectrum. Other peaks are washed away, forming a broad dispersive maximum above the Fermi level for momenta in the central part of the magnetic Brillouin zone. Simultaneously a maximum develops below the Fermi level (compare curves 2 and 3 in Fig. 2). As seen in Fig. 3, this maximum possesses dispersion and is comparatively narrow near the Fermi level.

The energy positions of the spectral maxima discussed above as functions of momentum are shown in Fig. 4 for heavily underdoped and moderately doped cases [as

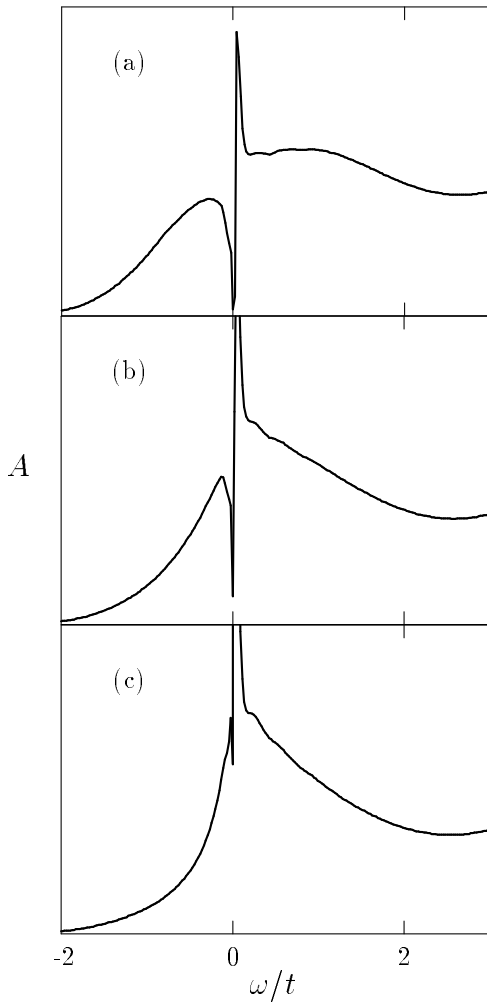


Fig. 3. The hole spectral function for  $\mathbf{k} = (0.5\pi, \pi)$  (a),  $(0.4\pi, \pi)$  (b), and  $(0.3\pi, \pi)$  (c).  $x = 0.133$ ,  $T = 0$ .

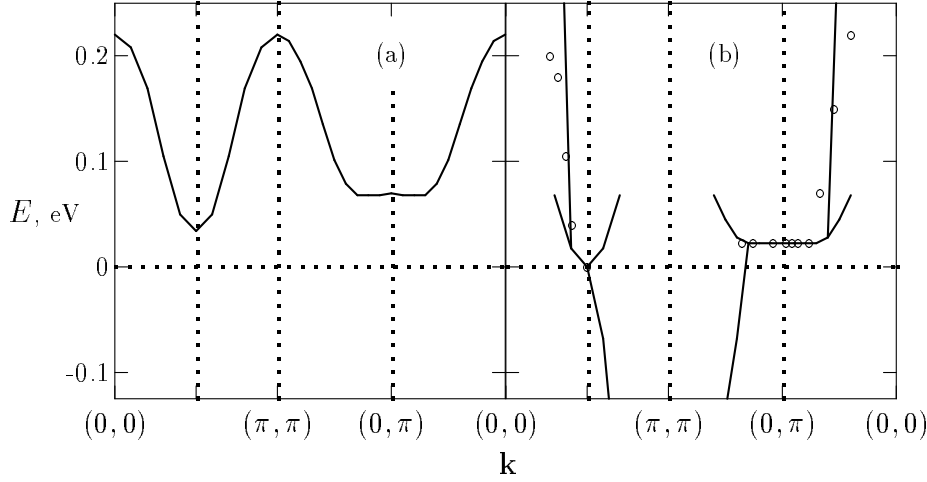


Fig. 4. Energy vs. momentum relationships calculated for  $x = 0.021$ ,  $T = 0$  (a) and  $x = 0.121$ ,  $T = 0.02t = 116$  K (b, solid line). In part (b), circles indicate positions of quasiparticle peaks in the photoemission experiment [40] carried out at  $T = 100$  K in a Bi2212 crystal with  $T_c = 85$  K.

discussed above, we have used the experimental fact that hole pockets are positioned around  $(\pm\pi, \pm\pi)$  to relate the portion of the energy band below the Fermi level to this part of the full Brillouin zone]. Figure 4a demonstrates the well-known spin-polaron band discussed in a large number of works devoted to the case of low doping (see, e.g., [32,33,36–39]). The width of this band is of the order of  $J$ , i.e. much less than the hole hopping constant  $t$ . This is connected with the above discussed fact that in the rigorous antiferromagnetic order the hole movement requires the emission and absorption of magnons. In such conditions the slower subsystem — magnons — will determine the bandwidth of the combined quasiparticle. As mentioned, a part of the spin-polaron band is retained near the boundary of the magnetic Brillouin zone for moderate doping. As seen in Fig. 4b, this part retains, with some distortion, main features of the spin-polaron band in this region. Among these features is the large nearly flat region which is visible around  $(0, \pi)$  in Fig. 4b. In this figure we have compared the calculated energy band with the normal-state photoemission data [40] in Bi2212 with  $T_c = 85$  K which corresponds to the hole concentration in the range  $0.11 - 0.15$ . In Ref. [40] the energy position of the flat region — the so-called extended van Hove singularity — is estimated to be  $\pm 30 - 50$  meV relative to the Fermi level. We positioned the experimental flat region at  $+20$  meV (in the hole picture), in accordance with later more exact measurements [3]. As seen in Fig. 4b, with respect to both the energy position and the extension in the Brillouin zone the calculations reproduce well the experimental van Hove singularity. Notice that also the general shape of the band, as seen in photoemission (which tests the region  $\omega \geq 0$ ), is well reproduced by the calculations. That the flat portion of the spin-polaron band can correspond to the photoemission extended saddle point was apparently first indicated in Ref. [41].

As follows from Fig. 4, considerable changes occur in the hole band shape on moving from light to moderate dopings, as was first indicated in Refs. [39,34]. The narrow, with

the width of the order of  $J$ , spin-polaron band is transformed to a much wider band characterized by the energy parameter  $t$ . The general shape of this band resembles a considerably distorted 2D nearest-neighbor band produced by the kinetic term of the  $t$ - $J$  Hamiltonian (3). Analogous changes in the band shape are observed in the photoemission of Bi2212 [2]. These changes point to a certain weakening of correlations for  $x > 0.04$ , however, some features of the strongly correlated spectrum are retained: as mentioned, near the Fermi level around the boundary of the magnetic Brillouin zone the spectrum contains a persistent part of the spin-polaron band and widths of spectral maxima grow steeply with distance from the Fermi level.

These changes in the hole spectrum are connected with changes in the magnon subsystem. For  $T = 0$  starting from  $x \approx 0.02$  in the central part of the magnetic Brillouin zone magnons become overdamped. The overdamped magnons manifest themselves in a perceptible intensity of the magnon spectral function  $B_{11}(\mathbf{k}\omega) = -\text{Im } D_{11}(\mathbf{k}\omega)$  in the nearest vicinity and on both sides of  $\omega = 0$  (see Fig. 5a where together with the structure corresponding to an overdamped magnon the maximum of a usual magnon is also visible; notice that overdamped magnons do not form maxima in  $B_{11}$  because this quantity changes sign at the central frequency  $\omega = 0$  of these magnons). The appearance of the overdamped magnons points to the destruction of the long-range antiferromagnetic order by holes [20,42] which, in contrast to the destruction due to thermal fluctuations, occurs also at zero temperature. Due to a finite intensity in  $B_{11}$ , produced by these magnons in the range  $\omega < 0$ , the magnon occupation number  $n_{\mathbf{k}} = -\int_{-\infty}^{\infty} d\omega \pi^{-1} n_B(\omega) B_{11}(\mathbf{k}\omega)$  is finite at  $T = 0$  which leads to a finite zero-temperature correlation length  $\xi$  in the spin correlation function  $\langle s_{\mathbf{l}}^z s_{\mathbf{m}}^z \rangle$  (in the considered finite lattice this phase transition is smeared; fortunately for relevant small  $x$  an analytic consideration for an infinite lattice is possible [20,42]). The overdamped magnons can be identified with relaxational modes describing relative rotations of magnetic quantization axes in regions of size  $\xi$ . In the hole spectrum the destruction of the long-range antiferromagnetic order manifests itself in the mentioned change of the shape and characteristic energy of the spectrum from  $J$  to  $t$  at  $x \approx 0.04$ . Qualitatively this can be understood in the following way: after the destruction of the long-range

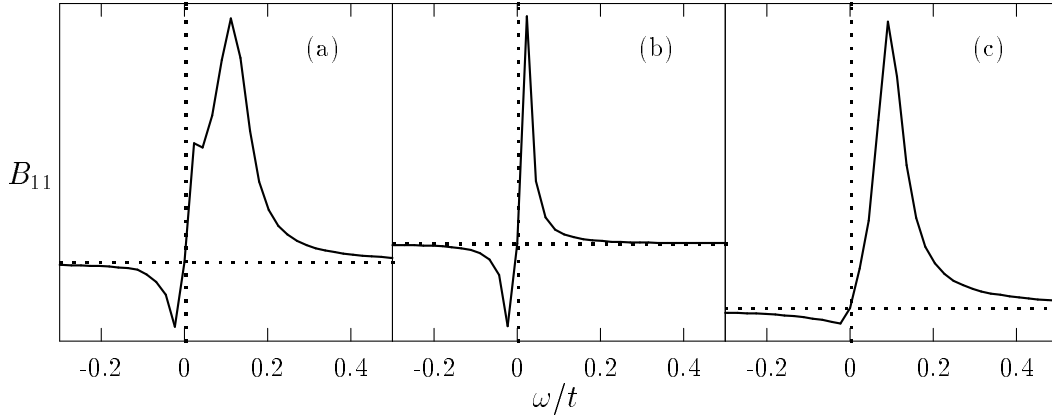


Fig. 5. The magnon spectral function  $B_{11}(\mathbf{k}\omega)$  for  $\mathbf{k} = (0, \pi/5)$ ,  $T = 0$ ,  $x = 0.059$  (a),  $\mathbf{k} = (0, 0)$ ,  $T = 58$  K,  $x = 0.1$  (b), and  $\mathbf{k} = (\pi/2, \pi/2)$ ,  $T = 116$  K,  $x = 0.172$  (c).

order holes can move without introducing additional disorder in the magnon subsystem and, as a result, the larger characteristic energy,  $t$ , reveals itself in the spectrum.

Apparently nearly simultaneously with the appearance of overdamped magnons  $\eta$  becomes finite and a gap opens in the magnon spectrum. The low-frequency overdamped magnons transform this gap to a pseudogap. This pseudogap is most evident in  $B_{11}(\mathbf{k} = 0, \omega)$  by the asymmetry of the spectrum around  $\omega = 0$  (Fig. 5b). In spite of the appearance of overdamped magnons, even at  $x \approx 0.17$  and  $T \approx 100$  K usual magnons with essentially softened frequencies and increased damping are retained at the periphery of the magnetic Brillouin zone indicating persistent antiferromagnetic correlations (see Fig. 5c).

Let us return to the hole spectrum. The hole Fermi surfaces calculated for moderate dopings are shown in Figs. 6a and 6b. In part (a), line segments along the boundary of the magnetic Brillouin zone are connected with the spin-polaron band. After touching the Fermi level (which occurs at  $x \approx 0.01$ ) the bottom of this band remains pinned to the Fermi level and the band flattens with increasing  $x$ . Originating from work [43] it is widely believed that for small hole concentrations the Fermi surface consists of small hole pockets around  $(\pm\pi/2, \pm\pi/2)$ . Our calculations do not support this point of view. The Fermi level does not cross the bottom of the spin-polaron band but is rather pinned to this bottom and the mentioned hole pockets do not arise [notice however that the line segments near  $(\pm\pi/2, \pm\pi/2)$  in Fig. 6 can have a finite width provided that it is much less than our momentum resolution  $\pi/10$ ].

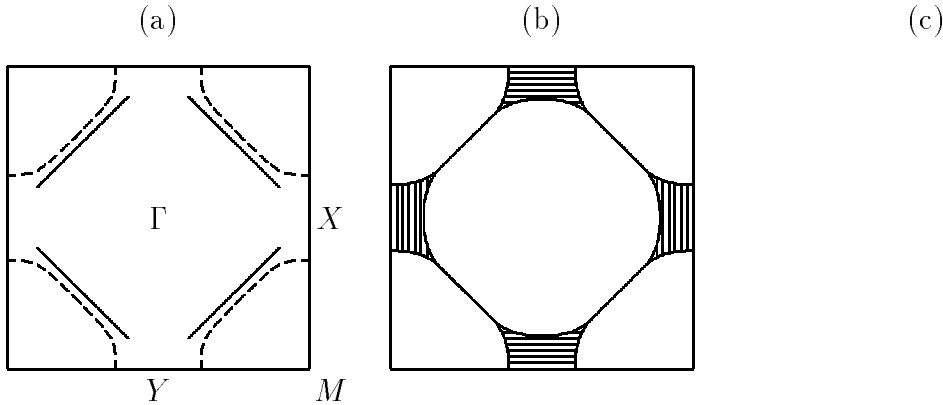


Fig. 6. The calculated hole Fermi surface for  $T \approx 100$  K,  $0.07 \lesssim x < 0.17$  (a),  $x = 0.172$  (b), and experimental Fermi surface for several cuprates (c, from Ref. [44]). Dashed lines in (a) and hatched regions in (b) indicate hidden and two-dimensional parts of the surface. The points  $X$ ,  $Y$ , and  $M$  correspond to  $\mathbf{k} = (\pi, 0)$ ,  $(0, -\pi)$ , and  $(\pi, \pi)$ , respectively.

In Fig. 6a, dashed curves indicate the crossings of the Fermi level by the part of the energy band which arises with growing  $x$  below the bottom of the spin-polaron band (see Figs. 2–4). This part forms hole pockets around  $(\pm\pi, \pm\pi)$  and determines the hole concentration (18). The pockets start to form from small  $x$  and their extent in the Brillouin zone grows with  $x$ ; however up to  $x \approx 0.07$  the pockets do not reach the Fermi level — all their states are positioned below the Fermi level. Thus, for  $x \lesssim 0.07$  the Fermi surface consists of only the line segments along the boundary

of the magnetic Brillouin zone and no closed Fermi surface exists. For larger hole concentrations the hole pockets reach the Fermi level and the crossings depicted by the dashed curves in Fig. 6a arise. However, as seen in Fig. 3, just at this crossing the weaker maximum corresponding to the pocket is completely lost within the foot of a much more intensive spin-polaron peak which is located somewhat above the Fermi level for the temperature, hole concentration and wave vectors of Fig. 3. Thus, the dashed curves in Fig. 6a correspond to hidden parts of the Fermi surface. If like in photoemission experiments the spectrum is not tested below the Fermi level (in the hole picture), the respective crossings reveal themselves only as a finite spectral intensity at the Fermi level.

As mentioned, with growing  $x$  the persistent part of the spin-polaron band flattens. As a consequence, the extended saddle points approach the Fermi level and at  $x = 0.172$  they fall on it. The Fermi surface of the considered two-dimensional fermions becomes two-dimensional, as shown in Fig. 6b. The mentioned hole concentration is close to optimal doping which corresponds to the highest  $T_c$ . As observed in photoemission of Bi2212 [2], in this case the saddle points do lie, within the experimental accuracy, on the Fermi level. Fig. 6c demonstrates Fermi surfaces deduced from photoemission in  $\text{Nd}_{2-x}\text{Ce}_x\text{CuO}_4$  (NCCO), Bi2212, and  $\text{Bi}_2(\text{Sr}_{0.97}\text{Pr}_{0.03})_2\text{CuO}_{6+\delta}$  (Bi2201). Contrasting this figure with Figs. 6a and 6b, we conclude that our calculations reproduce satisfactorily the main features of the experimental Fermi surface in crystals with significantly different hole concentrations.

For Fig. 6a we indicated the concentration range where the Fermi surface remains practically unchanged. In particular, it means that the size of the  $(\pm\pi, \pm\pi)$  hole pockets varies only slightly in the concentration range  $0.07 \lesssim x \lesssim 0.17$ . This result of our calculations agrees with experiment [1] and points to the substantial violation of Luttinger's theorem [45]. In accord with this theorem the area enclosed by the Fermi surface in the Brillouin zone should vary linearly with  $x$ . As seen in Fig. 2, quasiparticle weights of states (spectral intensities) which form the hole pockets grow with increasing  $x$ . It is this growth of quasiparticle weights, rather than the growing size of these pockets, which leads to the increase of the hole concentration in Eq. (18).

As follows from the above discussion, the energy spectrum of the considered fermions differs essentially from the Fermi liquid behavior of conventional metals. To this we can add the linear, rather than quadratic, frequency dependences of the hole decay widths near the Fermi level in the case of moderate doping [39]. This result resembles the marginal Fermi liquid [46], however, in contrast to this concept our calculated  $\text{Im } \Sigma(\omega)$  has markedly different slopes below and above the Fermi level and a strong momentum dependence.

## VI. PSEUDOGAP IN THE HOLE SPECTRUM

As follows from Fig. 3, the spin-polaron peak is the most prominent feature of the hole spectrum near the Fermi level for wave vectors in the vicinity of the Fermi surface. The hole spectral function is directly related to the photoemission spectrum. Hence the spin-polaron peak will determine the position of the leading edge of the photoemission

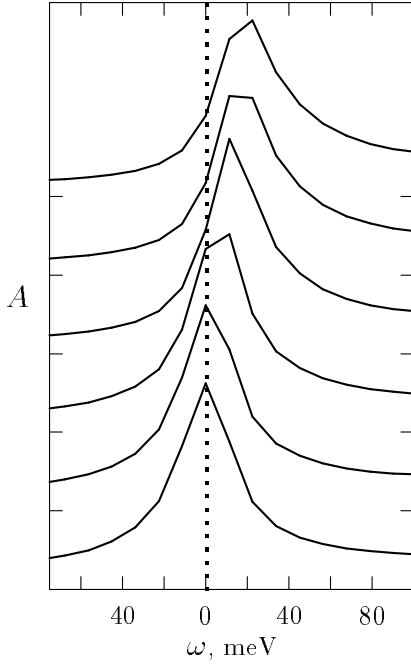


Fig. 7. The hole spectral function for wave vectors on the Fermi surface. Curves from top to bottom correspond to  $\mathbf{k} = (0.2\pi, \pi)$ ,  $(0.2\pi, 0.9\pi)$ ,  $(0.2\pi, 0.8\pi)$ ,  $(0.3\pi, 0.7\pi)$ ,  $(0.4\pi, 0.6\pi)$ , and  $(0.5\pi, 0.5\pi)$ , respectively.  $T = 116$  K,  $x = 0.121$ .

spectrum. For several wave vectors on the Fermi surface the hole spectral function is shown in Fig. 7 for the underdoped case. As seen from this figure, the spin-polaron maximum, which lies on the Fermi level near  $(\pi/2, \pi/2)$ , is shifted upwards on approaching  $(\pi/5, \pi)$ . Recall that the part of the Fermi surface near  $(\pi/5, \pi)$  is connected with another, broader and weaker maximum which is completely lost at the foot of the spin-polaron peak on crossing the Fermi level (see Fig. 3). As a consequence, the situation in Fig. 7 looks like a part of the Fermi surface disappears and a gap opens between the hole energy band and the Fermi level near  $(\pi/5, \pi)$ . Due to the mentioned hidden crossing of the Fermi level in this point there remains a finite intensity at  $\omega = 0$  which transforms the gap to the pseudogap. The same behavior of the leading edge is observed in photoemission of underdoped cuprates which led to the idea of the photoemission pseudogap [1–3].

In Fig. 8 we compare our calculated position of the spin-polaron peak and the experimentally measured position of the photoemission leading edge [3] as functions of momentum along the Fermi surface shown in the insets of both parts of the figure (some differences in the Fermi surfaces shown may be connected both with the experimental resolution which produces some uncertainty in the position of the Fermi surface especially in the case of narrow bands and with the influence of terms not included in the  $t$ - $J$  Hamiltonian). In part (b), the location on the Fermi surface is determined by the angle measured from the line  $(\pi, \pi) - (\pi, 0)$ . At  $T = 14$  K experimental curves for the 83 K and 87 K samples in Fig. 8b correspond to superconducting gaps. As indicated in Ref. [3], in the former, underdoped sample the shape of the curve and the magnitude of the gap remain practically unchanged when the temperature increases and somewhat exceeds  $T_c$ , while the gap is closed in the latter, optimally doped sample. Taking into account these experimental facts we conclude from the comparison of Figs. 8a and 8b that the calculations reproduce satisfactorily the general shape and the magnitude of



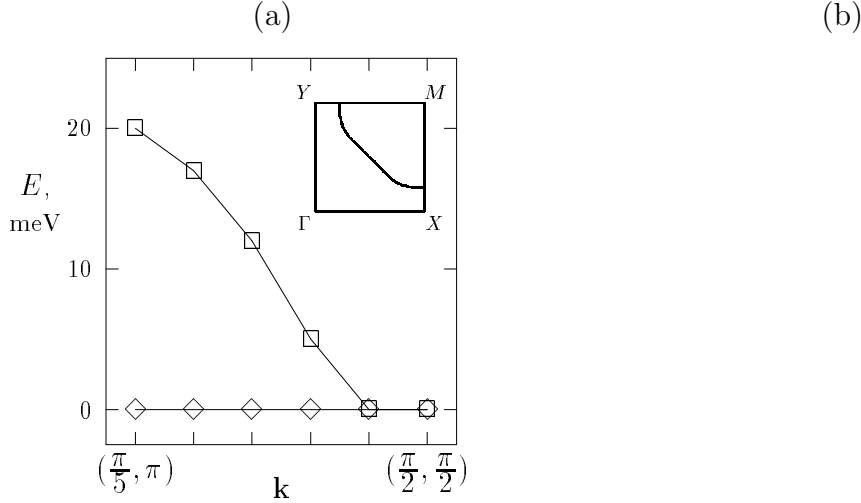


Fig. 8. (a) The position of the spin-polaron peak along the Fermi surface, shown in the inset, for  $x = 0.121$  ( $\square$ ) and  $x = 0.172$  ( $\diamond$ ) at  $T = 116$  K. The points  $M$ ,  $X$ , and  $Y$  are defined in the caption of Fig. 6. (b) The position of the leading edge of the photoemission spectrum vs. momentum along the Fermi surface in the inset for samples with  $T_c = 10$  K (heavily underdoped, triangles), 83 K (underdoped, squares), and 87 K (optimally doped, circles). Measurements in Ref. [3], where this figure were taken from, were carried out for Bi2212 at  $T = 14$  K. The points  $\overline{M}$  and  $Y$  correspond to the  $X$ ,  $Y$  and  $M$  points in the square Brillouin zone.

the normal-state pseudogap in the underdoped case. Moreover, as seen from Fig. 8a, in agreement with experiment the pseudogap is closed in the case of optimal doping.

In Ref. [3] the similarity of symmetries of the superconducting gap and the normal-state pseudogap and their smooth evolution into each other with temperature served as the basis for the supposition that the pseudogap is the normal-state precursor of the superconducting gap. In accord with this supposition the pseudogap arises above  $T_c$  due to superconducting fluctuations. We did not include these fluctuations in our present calculations and thus the pseudogap shown in Fig. 8a is not connected with the fluctuations. In our calculations the pseudogap arises due to the specific dispersion of the spin-polaron band, a part of which is retained near the Fermi level at moderate doping and gives the most intensive maxima in the spectral function. The existence of this band is a consequence of strong electron correlations. We do not exclude the possibility that the superconducting fluctuations do contribute to the pseudogap, however, based on the satisfactory agreement between our estimate and the observed pseudogap magnitude we suppose that the main contribution is provided by strong electron correlations. Besides, with the superconducting fluctuation mechanism it is difficult to understand why the pseudogap appears only on one side of the Fermi level and why the fluctuations disappear abruptly in a small concentration range near optimal doping when the pseudogap is closed. For the 2D  $t$ - $J$  model various calculations (see, e.g., Refs. [34,47–49]) give the  $d_{x^2-y^2}$  symmetry for the superconducting gap in the case of moderate doping. This gap looks similar to the pseudogap in Fig. 8a, as the symmetries of both of them are determined by the hole-magnon interaction and by short-range

antiferromagnetic ordering. This ensures smooth evolution of the pseudogap into the superconducting gap with lowering temperature below  $T_c$ .

As observed in Ref. [3], in slightly underdoped samples the pseudogap is closed when temperature exceeds some  $T^*$ . This characteristic temperature increases steeply with decreasing hole concentration. We believe that this behaviour is connected with crossing the boundary shown in Fig. 1. Outside of this boundary for  $x \gtrsim 0.12$  we found a hole energy spectrum which is similar to the spectrum of the usual metal and does not contain any pseudogap.

Concluding this section let us mention two differences we see between our calculated and the experimental results. First, in our calculations the magnitude of the pseudogap increases slightly with decreasing hole concentration, while in the experiment [3] it remains unchanged, within experimental errors, for samples with markedly different  $x$  (see Fig. 8b). Second, in the normal-state photoemission spectra of underdoped Bi2212 the linewidth increases dramatically on moving from  $(\pi/2, \pi/2)$  to the vicinity of  $(0, \pi)$  [2]. Though the photoemission line shape is not well understood [50], an analogous behavior of linewidths could be expected in the hole spectral function. However, in our results in Fig. 7 the change of the linewidth does not look so dramatic. This contradiction points either to the experimental pseudogap being somewhat larger than that reported in Ref. [3] [in this case the overdamped magnons wash away the  $(0, \pi)$  maximum, as they did with the  $(0, 0)$  maximum in Fig. 2a, curve 2] or to some decay process with low-frequency excitations not included in the  $t$ - $J$  model.

## VII. MAGNETIC PROPERTIES

The spin correlation function  $C_{\mathbf{l}-\mathbf{m}} = \langle s_{\mathbf{l}}^z s_{\mathbf{m}}^z \rangle$  is given by

$$C_{\mathbf{l}-\mathbf{m}} = -\frac{1}{4}\delta_{\mathbf{ml}} + \left\{ \frac{2}{N} \sum_{\mathbf{k}}' \frac{e^{i\mathbf{k}(\mathbf{m}-\mathbf{l})}}{\sqrt{1-\eta^2\gamma_{\mathbf{k}}^2}} \left[ \langle b_{\mathbf{k}\sigma}^\dagger b_{\mathbf{k}\sigma} \rangle_U + \frac{1}{2} - \eta\gamma_{\mathbf{k}} \langle b_{-\mathbf{k},-\sigma} b_{\mathbf{k}\sigma} \rangle_U \right] \right\}^2 \quad (19a)$$

when  $\mathbf{l}$  and  $\mathbf{m}$  belong to the same sublattice and

$$C_{\mathbf{l}-\mathbf{m}} = -\left\{ \frac{2}{N} \sum_{\mathbf{k}}' \frac{e^{i\mathbf{k}(\mathbf{m}-\mathbf{l})}}{\sqrt{1-\eta^2\gamma_{\mathbf{k}}^2}} \left[ \langle b_{-\mathbf{k},-\sigma} b_{\mathbf{k}\sigma} \rangle_U - \eta\gamma_{\mathbf{k}} \left( \langle b_{\mathbf{k}\sigma}^\dagger b_{\mathbf{k}\sigma} \rangle_U + \frac{1}{2} \right) \right] \right\}^2 \quad (19b)$$

when  $\mathbf{l}$  and  $\mathbf{m}$  are on different sublattices. In the considered region of the  $T$ - $x$  plane the decay of spin correlations (19) with the distance  $|\mathbf{l} - \mathbf{m}|$  is nonexponential (see Fig. 9) which may be partly connected with finite-size effects. To estimate the spin correlation length we used the formula

$$\xi^2 = \sum_{\mathbf{l}} |\mathbf{l}|^2 e^{i\mathbf{l}\mathbf{m}} \langle s_{\mathbf{l}}^z s_{\mathbf{0}}^z \rangle / (2 \sum_{\mathbf{l}} e^{i\mathbf{l}\mathbf{m}} \langle s_{\mathbf{l}}^z s_{\mathbf{0}}^z \rangle).$$

For  $T = 116$  K the product  $\xi\sqrt{x}$  is nearly constant and approximately equal to the lattice spacing in the range  $0.017 \lesssim x \lesssim 0.09$ , in agreement with experiment in  $\text{La}_{2-x}\text{Sr}_x\text{CuO}_4$  [26]. For larger  $x$  at this temperature,  $\xi$  becomes of the order of the

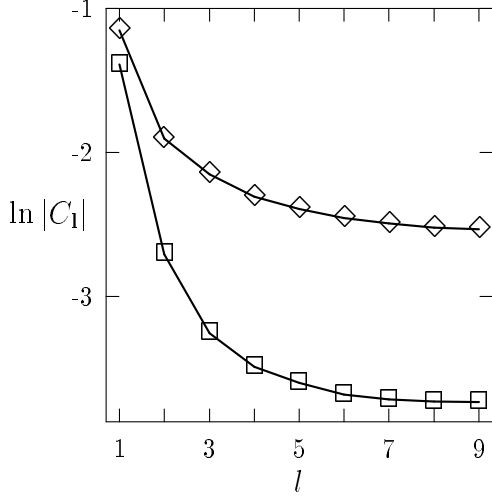


Fig. 9. The spin correlation function along the lattice axis  $[\mathbf{l} = (l, 0)]$  for  $x = 0.027$  ( $\diamond$ ) and  $x = 0.1$  ( $\square$ ) at  $T = 0$ .

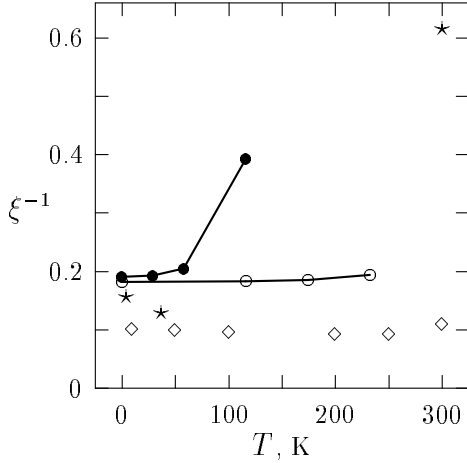


Fig. 10. The inverse correlation length in units of the inverse lattice spacing for  $x \approx 0.03$  (open circles) and  $x \approx 0.1$  (filled circles). Values obtained from the neutron-scattering experiments in  $\text{La}_{1.86}\text{Sr}_{0.14}\text{CuO}_4$  [51] and in  $\text{La}_{1.96}\text{Sr}_{0.04}\text{CuO}_4$  [26] are shown by stars and diamonds, respectively.

lattice spacing. As mentioned, the use of the spin-wave approximation (7) assumes that  $\xi \gg a$ . We hope, however, that our results obtained for the case  $\xi \approx a$  (the region near the curve in Fig. 1 for  $x > 0.09$ ) may give at least qualitatively a correct description of this region. When  $x \lesssim 0.06$ , our calculated  $\xi$  is nearly independent of temperature in the considered range of  $T$ , as seen in Fig. 10 for the case  $x \approx 0.03$  (for fixed  $\mu$  the hole concentration is somewhat changed with  $T$ ; values of  $x$  given in the figure captions here and below are mean values for the considered temperature ranges). This behaviour agrees with experimental data in  $\text{La}_{1.96}\text{Sr}_{0.04}\text{CuO}_4$  [26], also shown in Fig. 10. For larger  $x$  values  $\xi^{-1}$  are also weakly temperature-dependent at low  $T$  and increase more rapidly as the boundary in Fig. 1 is approached (see the data for  $x \approx 0.1$  in Fig. 10). This behaviour is also in agreement with experimental results in  $\text{La}_{1.86}\text{Sr}_{0.14}\text{CuO}_4$  by G. Aeppli et al. reported in Ref. [51] (stars in Fig. 10). Notice, however, that the growth of  $\xi^{-1}$  predicted by the theory is somewhat more rapid than that observed in experiment. The saturation of  $\xi$  with decreasing  $T$ , demonstrated by Fig. 10, is the distinctive property of the quantum disordered regime [14,28] in which the system resides in the considered region of the  $T$ - $x$  plane.

In this region the hole contribution  $\chi_h^z$  to the susceptibility is negligibly small in

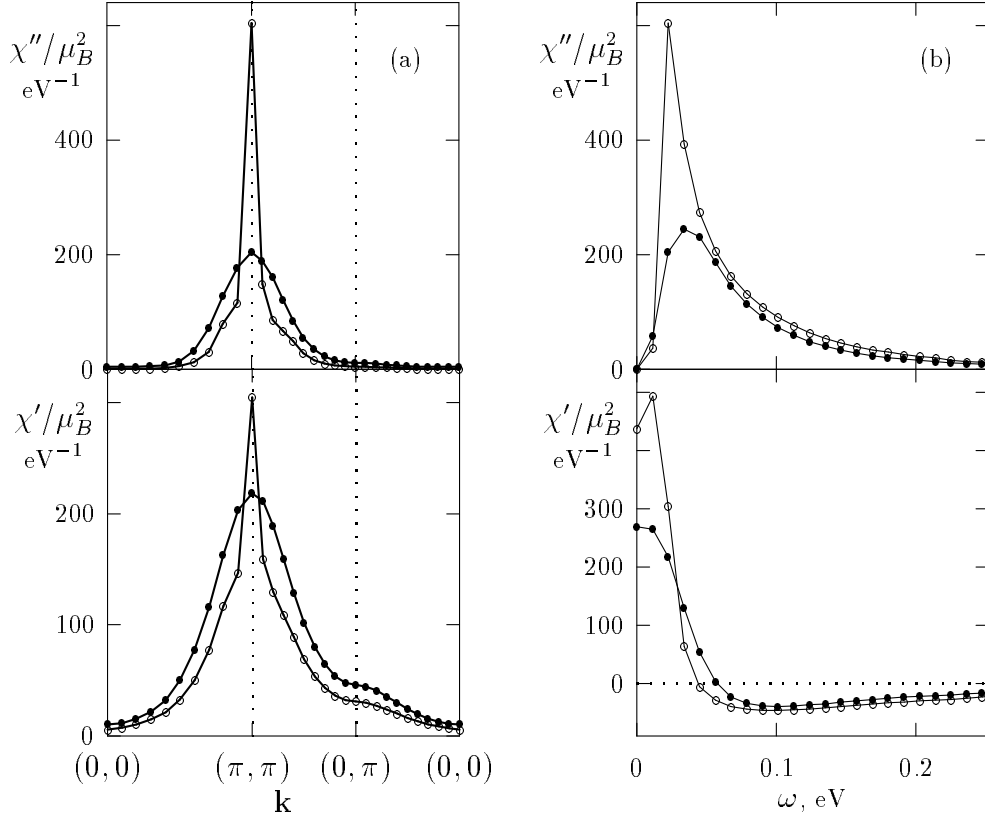


Fig. 11. Imaginary  $\chi''$  and real  $\chi'$  parts of the magnetic susceptibility as functions of wave vector along the symmetry lines in the Brillouin zone for  $\omega \approx 0.022$  eV (a) and frequency for  $\mathbf{k} = (\pi, \pi)$  (b).  $x \approx 0.11$ . Open and filled circles correspond to  $T = 58$  K and 116 K, respectively.

comparison with the spin contribution  $\chi_m^z$ . As seen in Fig. 11, the magnetic susceptibility (16) is strongly peaked around  $(\pi, \pi)$ . This demonstrates strong antiferromagnetic fluctuations which persist even in the case of comparatively short correlation lengths of the order of the lattice spacing. As known, low-frequency incommensurate spin fluctuations are observed in the normal state of Sr-doped  $\text{La}_2\text{CuO}_4$  [52]. This becomes apparent in a four-peaked structure of  $\text{Im} \chi(\mathbf{q}\omega)$ , the peaks being displaced from the commensurate position to the points  $\mathbf{q}_i = (\pi, \pi \pm \delta)$ ,  $(\pi \pm \delta, \pi)$ . To investigate whether this incommensurability is connected with the hole-magnon interaction in  $\text{CuO}_2$  planes a more sophisticated spin-wave approximation than that given in Eq. (7) is needed. We do not consider this point in the present paper. Notice that the frequency dependence of  $\text{Im} \chi(\mathbf{q}\omega)$  in Fig. 11b is close to that observed in normal-state  $\text{La}_{1.86}\text{Sr}_{0.14}\text{CuO}_4$  at wave vectors  $\mathbf{q}_i$  [51]. Both the total peak intensity at these wave vectors, the position of the peak, and its temperature dependence are close to those shown in this figure.

We used the obtained magnetic susceptibility for calculating the spin-lattice relaxation times at the Cu and O sites  $^{67}\text{T}_1$  and  $^{17}\text{T}_1$  and the Cu spin-echo decay time  $T_{2G}$  by using the equations [14]

$$\frac{1}{\alpha T_1 T} = \frac{1}{2\mu_B^2 N} \sum_{\mathbf{q}} \alpha F(\mathbf{q}) \frac{\text{Im} \chi(\mathbf{q}\omega)}{\omega}, \quad \omega \rightarrow 0,$$

$$\frac{1}{T_{2G}} = \sqrt{\frac{0.69}{128}} \left( {}^{63}\gamma_n \right)^2 \left\{ \frac{1}{N} \sum_{\mathbf{q}} F_e^2(\mathbf{q}) [\text{Re} \chi(\mathbf{q}0)]^2 - \left[ \frac{1}{N} \sum_{\mathbf{q}} F_e(\mathbf{q}) \text{Re} \chi(\mathbf{q}0) \right]^2 \right\}^{1/2}, \quad (20)$$

$${}^{63}F(\mathbf{q}) = [A_{\perp} + 4B\gamma_{\mathbf{q}}]^2, \quad F_e(\mathbf{q}) = [A_{\parallel} + 4B\gamma_{\mathbf{q}}]^2, \quad {}^{17}F(\mathbf{q}) = 2C^2 [1 + \cos(q_x)]^2,$$

where  ${}^{63}\gamma_n$  is the Cu nucleus gyromagnetic ratio,  $B = 3.82 \cdot 10^{-7}$  eV,  $A_{\perp} = 0.84B$ ,  $A_{\parallel} = -4B$ , and  $C = 0.91B$ . The spin-lattice relaxation times in Eq. (20) correspond to the applied static magnetic field perpendicular to the  $\text{CuO}_2$  plane. Results are shown in Fig. 12 together with the calculated  $\chi^0 = \chi(0,0)$  and the respective experimental results obtained in  $\text{YBa}_2\text{Cu}_3\text{O}_{6.63}$  [14,53,54]. From our results for different hole concentrations we selected for this figure those which appeared to be closest to the experimental data.

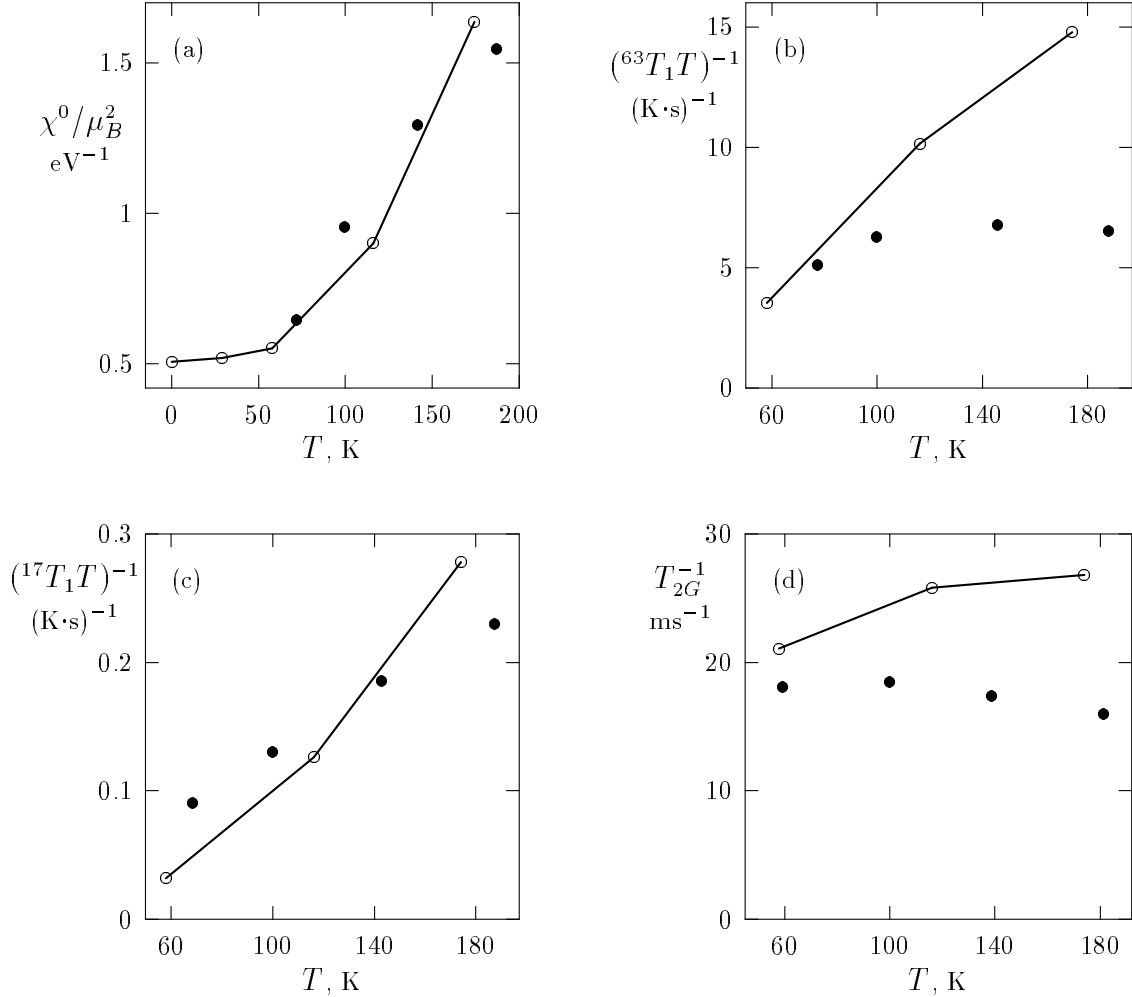


Fig. 12. The static spin susceptibility (a),  $1/(T_1 T)$  at the Cu (b) and O (c) sites for  $\mathbf{H} \parallel \mathbf{c}$ , and  $1/T_{2G}$  (d) calculated for  $x \approx 0.05$  (open circles). The experimental data for  $\text{YBa}_2\text{Cu}_3\text{O}_{6.63}$  are shown by filled circles.  $\chi^0$  was inferred from the Knight shift data [14],  $1/(T_1 T)$  and  $1/T_{2G}$  are from Refs. [53] and [54], respectively.

Those results are for  $x \approx 0.05$  which is apparently somewhat smaller than the hole concentration in  $\text{YBa}_2\text{Cu}_3\text{O}_{6.63}$ . With increasing  $x$  our calculated  $\chi^0$  and  $(^aT_1T)^{-1}$  increase, remaining of the same order of magnitude as those shown in Fig. 12, while  $T_{2G}^{-1}$  slightly decreases. These concentration dependences of  $\chi^0$  and  $T_{2G}^{-1}$  agree with experimental observations [14,54–56], though for  $\chi^0$  the theoretical dependence is stronger than that observed experimentally. The situation is apparently more difficult for  $(^{63}T_1T)^{-1}$ . In underdoped  $\text{YBa}_2\text{Cu}_3\text{O}_{6+y}$  this quantity decreases with doping [57], while in  $\text{HgBa}_2\text{CuO}_{4+\delta}$ , it increases [58]. Apparently a more elaborate model is necessary for the description of this concentration dependence. Analyzing Fig. 12 we conclude that the  $t$ - $J$  model is able to describe correctly the temperature dependences of the depicted quantities and to give their proper orders of magnitude in the quantum disordered regime.

As seen in Fig. 12,  $(T_1T)^{-1}$  and  $\chi^0$  decrease with decreasing temperature. Such behaviour observed for  $T > T_c$  in underdoped cuprates [4,5] is considered as an indication of the pseudogap in the spectrum of magnetic excitations [4,5,13,14]. Our results corroborate this point of view — analyzing Eq. (16) and our numerical data we came to the conclusion that the mentioned temperature dependence is mainly connected with the occupation of low-frequency magnons, rather than the temperature variation of the magnon spectral intensities. Due to the pseudogap this occupation decreases with temperature.

## VIII. SUMMARY

In this work we applied the modified spin-wave theory with the additional constraint of zero staggered magnetization to the two-dimensional  $t$ - $J$  model in the paramagnetic state. In the Born approximation the constraint equation (12) and the self-energy equations (17) for the hole and magnon Green's functions form the self-consistent set which was solved numerically for finite hole concentrations  $x$  and temperatures  $T$ . The constraint can be fulfilled in the region of the  $T$ - $x$  plane below the curve in Fig. 1.

A number of unusual features of photoemission spectra in cuprate perovskites are satisfactorily reproduced by the obtained results. Among these features are the general shape of the electron energy spectrum and its evolution from the narrow spin-polaron band at small doping to the much wider band for moderate doping. Both by the energy position and by the extension in the Brillouin zone our calculated extended saddle point reproduces well the van Hove singularity of photoemission spectra. Also the obtained Fermi surface with hidden and two-dimensional parts is close to that observed experimentally. In the calculated Fermi surface the size of the hole pockets varies only slightly with the growth of the hole concentration. This growth is mainly connected with an increase of the quasiparticle weights of states occupied by holes. In our calculated hole spectrum the pseudogap has the magnitude, symmetry and the concentration dependence which are similar to those observed in photoemission. This pseudogap is not connected with superconducting fluctuations which were not included in the calculations. It arises due to the specific dispersion of the spin-polaron band a part of which is retained near the Fermi level at moderate doping and gives the most

intensive maxima in the spectral function. The persistence of this band is an indication of strong electron correlations retained at moderate doping.

We calculated also a number of magnetic characteristics of the  $t$ - $J$  model. We found that in the region shown in Fig. 1 the temperature variation of the spin correlation length is typical for the quantum disordered regime and that this dependence as well as the concentration dependence of the correlation length are close to those observed in cuprates. The magnon spectrum contains the pseudogap which manifests itself in the temperature dependence of the static spin susceptibility and spin-lattice relaxation rates at the Cu and O sites. Our calculated values of these quantities and the Cu spin-echo decay rate, their temperature and concentration dependences are in qualitative and in some cases in quantitative agreement with experiment.

The considered phase with the above-discussed properties differs essentially from the conventional metal. As mentioned, this phase exists in the region bounded by the curve in Fig. 1. Outside of this region for  $x \gtrsim 0.12$  we found the energy spectrum of the usual metal.

#### ACKNOWLEDGMENTS

This work was partially supported by the ESF grant No. 2688 and by the WTZ grant (Project EST112.1) of the BMBF.

## REFERENCES

- [1] A. G. Loeser, D. S. Dessau, and Z.-X. Shen, *Physica C* 263 (1996) 208.
- [2] D. S. Marshall, D. S. Dessau, A. G. Loeser, C.-H. Park, A. Y. Matsuura, J. N. Eckstein, I. Bozovic, P. Fournier, A. Kapitulnik, W. E. Spicer, and Z.-X. Shen, *Phys. Rev. Lett.* 76 (1996) 4841.
- [3] H. Ding, T. Yokoya, J. C. Campuzano, T. Takahashi, M. Randeria, M. R. Norman, T. Mochiku, K. Kadowaki, and J. Giapintzakis, *Nature* 382 (1996) 51.
- [4] T. Imai, H. Yasuoka, T. Shimizu, Y. Ueda, K. Yoshimura, and K. Kosuge, *Physica C* 162-164 (1989) 169.
- [5] J. Rossat-Mignod, L. P. Regnault, P. Bourges, P. Burlet, C. Vettier, and J. Y. Henry, *Physica B* 192 (1993) 109.
- [6] J. Maly, K. Levin, and D. Z. Lin, *Phys. Rev. B* 54 (1996) R15657.
- [7] R. S. Markiewicz, *J. Phys. Chem. Solids* 58 (1997) 1179.
- [8] N. Kristoffel and T. Örd, *Physica C* 298 (1998) 37.
- [9] N. Trivedi and M. Randeria, *Phys. Rev. Lett.* 75 (1995) 312.
- [10] V. Emery and S. A. Kivelson, *Nature* 374 (1995) 434.
- [11] A. Sherman and M. Schreiber, *Phys. Rev. B* 55 (1997) R712.
- [12] A. V. Chubukov and S. Sachdev, *Phys. Rev. Lett.* 71 (1993) 169.
- [13] A. Sokol and D. Pines, *Phys. Rev. Lett.* 71 (1993) 2813.
- [14] V. Barzykin and D. Pines, *Phys. Rev. B* 52 (1995) 13585.
- [15] V. M. Loktev and S. G. Sharapov, preprint cond-mat 9706285.
- [16] Yu. A. Izyumov, *Uspekhi Fiz. Nauk* 167 (1997) 465 [*Phys.-Usp. (Russia)* 40 (1997) 445].
- [17] M. Takahashi, *Phys. Rev. B* 40 (1989) 2494.
- [18] S. Tang, M. E. Lazzouni, and J. E. Hirsch, *Phys. Rev. B* 40 (1989) 5000.
- [19] A. Sherman and M. Schreiber, *Phys. Lett. A* 238 (1998) 303; *Physica C*, in press.
- [20] A. Sherman and M. Schreiber, *Phys. Rev. B* 48 (1993) 7492.
- [21] V. J. Emery, *Phys. Rev. Lett.* 58 (1987) 2794.
- [22] A. V. Sherman, *Phys. Rev. B* 47 (1993) 11521; *Physica C* 211 (1993) 329.
- [23] A. K. McMahan, J. F. Annett, and R. M. Martin, *Phys. Rev. B* 42 (1990) 6268.
- [24] J. H. Jefferson, H. Eskes, and L. F. Feiner, *Phys. Rev. B* 45 (1992) 7959.
- [25] S. V. Tyablikov, *Methods of the Quantum Theory of Magnetism* (Plenum Press, New York, 1967).
- [26] B. Keimer, N. Belk, R. G. Birgeneau, A. Cassanho, C. Y. Chen, M. Greven, M. A. Kastner, A. Aharony, Y. Endoh, R. W. Erwin, and G. Shirane, *Phys. Rev. B* 46 (1992) 14034.
- [27] D. A. Arovas and A. Auerbach, *Phys. Rev. B* 38 (1988) 316.
- [28] S. Chakravarty, B. I. Halperin, and D. R. Nelson, *Phys. Rev. B* 39 (1989) 2344.
- [29] S. Tyč and B. I. Halperin, *Phys. Rev. B* 42 (1990) 2096.
- [30] S. Schmitt-Rink, C. M. Varma, and A. E. Ruckenstein, *Phys. Rev. Lett.* 60 (1988) 2793.
- [31] C. L. Kane, P. A. Lee, and N. Read, *Phys. Rev. B* 39 (1989) 6880.
- [32] F. Marsiglio, A. E. Ruckenstein, S. Schmitt-Rink, and C. M. Varma, *Phys. Rev. B* 43 (1991) 10882.
- [33] G. Krier and G. Meissner, *Ann. Phys.* 2 (1993) 738.



- [34] A. Sherman, Phys. Rev. B 55 (1997) 582.
- [35] A. P. Kampf and J. R. Schrieffer, Phys. Rev. B 42 (1990) 7967.
- [36] A. V. Sherman, Physica C 171 (1990) 395.
- [37] G. Martinez and P. Horsch, Int. J. Mod. Phys. B 5 (1991) 207.
- [38] N. M. Plakida, V. S. Oudovenko, and V. Yu. Yushankhai, Phys. Rev. B 50 (1994) 6431.
- [39] A. Sherman and M. Schreiber, Phys. Rev. B 50 (1994) 12887.
- [40] Z.-X. Shen and D. S. Dessau, Phys. Repts. 253 (1995) 1.
- [41] E. Dagotto, A. Nazarenko, and M. Boninsegni, Phys. Rev. Lett. 73 (1994) 728.
- [42] F. Onufrieva, V. Kushnir, and B. Toperverg, Physica B 194-196 (1994) 1449.
- [43] B. I. Shraiman and E. D. Siggia, Phys. Rev. Lett. 60 (1988) 740.
- [44] D. M. King, Z.-X. Shen, D. S. Dessau, D. S. Marshall, C. H. Park, W. E. Spicer, J. L. Peng, Z. Y. Li, and R. L. Greene, Phys. Rev. Lett. 73 (1994) 3298.
- [45] J. M. Luttinger and J. C. Ward, Phys. Rev. 118 (1960) 1417; J. M. Luttinger, Phys. Rev. 119 (1960) 1153.
- [46] C. M. Varma, P. B. Littlewood, S. Schmitt-Rink, E. Abrahams, and A. E. Ruckenstein, Phys. Rev. Lett. 63 (1989) 1996.
- [47] D. J. Scalapino, Phys. Repts. 250 (1995) 329.
- [48] A. Sherman and M. Schreiber, Phys. Rev. B 52 (1995) 10621; Physica C 253 (1995) 23.
- [49] N. M. Plakida, Phil. Mag. B 76 (1997) 771; N. M. Plakida, V. S. Oudovenko, P. Horsch, A. I. Liechtenstein, Phys. Rev. B 55 (1997) R11997.
- [50] L. Z. Liu, R. O. Anderson, and J. W. Allen, J. Phys. Chem. Solids 52 (1991) 1473.
- [51] Y. Zha, V. Barzykin, and D. Pines, Phys. Rev. B 54 (1996) 7561.
- [52] G. Aeppli, S. M. Hayden, H. A. Mook, T. E. Mason, A. D. Taylor, K. N. Clausen, T. G. Perring, S.-W. Cheong, Z. Fisk, and D. Rytz, Physica B 192 (1993) 103.
- [53] M. Takigawa, A. P. Reyes, P. C. Hammel, J. D. Thompson, R. H. Heffner, Z. Fisk, and K. C. Ott, Phys. Rev. B 43 (1991) 247.
- [54] M. Takigawa, Phys. Rev. B 49 (1994) 4158.
- [55] R. E. Walstedt, R. F. Bell, L. F. Schneemeyer, J. V. Waszczak, and G. P. Espinosa, Phys. Rev. B 45 (1992) 8074.
- [56] T. Imai and C. P. Slichter, Phys. Rev. B 47 (1993) 9158.
- [57] C. Berthier, M.-H. Julien, O. Bakharev, M. Horvatić, and P. Ségransan, Physica C 282-287 (1997) 227.
- [58] H. Yasuoka, Physica C 282-287 (1997) 119.